Backshell radiation measurements in the EAST facility for Titan entry

Augustin Tibere-Inglesse[1]
NASA Postdoctoral Fellow at NASA Ames Research Center, Mountain View, CA, 94035, USA

Christopher O. Johnston[2]
NASA Langley Research Center, Hampton, VA, 23669, USA

Aaron M. Brandis[3]
NASA Ames Research Center, Mountain View, CA, 94035, USA

Brett A. Cruden[4]
AMA Inc at NASA Ames Research Center, Mountain View, CA, 94035, USA

A new test series was performed in the Electric Arc Shock Tube (EAST) facility, with the aim of reproducing conditions which will be encountered in the backshell of the Dragonfly spacecraft. Measurements of shock-layer radiation from CN Violet, CN Red and C_2 Swan bands are made in mixtures of 2.2% CH_4 in N_2 (by mole) heated by incident shock waves spanning from 3 to 7 km/s. This study focuses on the spectrally and spatially resolved measurement of absolute radiance made with four optical emission spectrometers spanning 220-1400 nm. Comparison with CFD simulations and equilibrium conditions were made. The predicted radiation was found to be between -40% to 100% from the measurements for the nonequilibrium peak radiance, increasing with velocity. At 7 cm/150 µs from the shock front, the discrepancies appear to be larger, ranging from -50 to 200%. Comparison between measured and predicted temperatures and number densities of CN indicate shortcomings in the non-Boltzmann model of CN.

I. Introduction

The Dragonfly mission involves a hypersonic entry into the atmosphere of Titan, Saturn's largest moon. Aerothermodynamic analysis predicts radiation to be an important source of heating on the backshell surface [1]. The main source of radiation is expected to come from the nonequilibrium radiation of CN via two transitions, one in the Ultraviolet region – $CN(B^2\Sigma^+ \rightarrow X^2\Sigma^+)$, also referred as CN(Violet) – and the other

[1] Postdoctoral Fellow, Aerothermodynamics Branch
[2] Senior Research Scientist, Aerothermodynamics Branch, and Associate Fellow AIAA.
[3] Senior Research Scientist, Aerothermodynamics Branch, and Associate Fellow AIAA.
[4] Senior Research Scientist, Aerothermodynamics Branch, and Associate Fellow AIAA.

in visible region – CN($A^2\Pi \rightarrow X^2\Sigma^+$), also referred as CN(Red) [2]. Reproduction of flight conditions in ground test facilities is of interest for heatshield design and to provide additional data that allows validation of predictive models. Such test campaigns have been performed previously in both NASA's Electric Arc Shock Tube (EAST) [3] [2] and University of Queensland's X2 shock tube [4, 5]. Both test series focused on stagnation point radiation which does not provide sufficient characterization of the conditions encountered by the backshell. The main conclusions of the EAST test campaigns are summarized in Figure 1, where T61 represents the data obtained and T45 is legacy test data deemed to be inaccurate. For CN(Violet), the measured peak radiance of T61 was correctly predicted. However, the predicted decay rate is always slower than measured. On the other hand, the peak radiance of CN(Red) is underestimated, but its decay rate is well predicted.

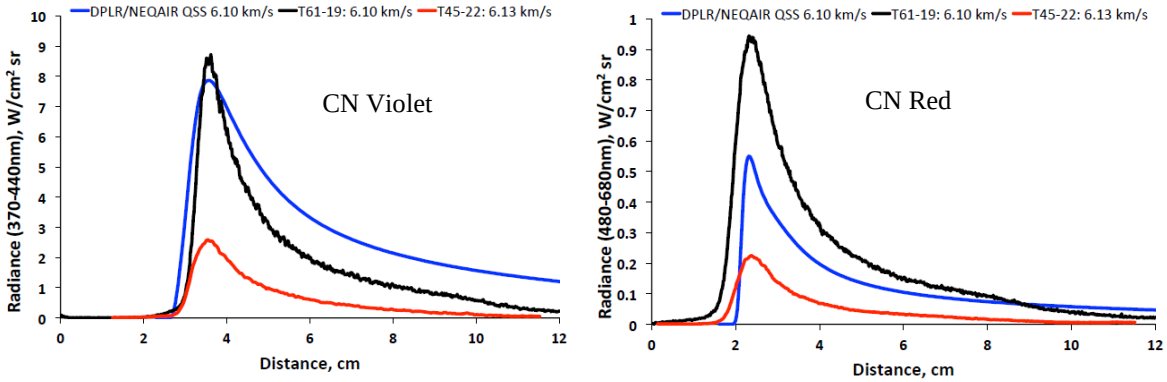

Figure 1: Comparison between simulated (Blue) and two experimental EAST test campaigns (Black and Red) radiance profiles of CN Violet (right) and CN Red (left) for a Titan's entry. Figures are taken from Ref. [2]

It has been recently shown that the radiation on the backshell of a capsule could be modeled by the radiation of an equivalent oblique shock for Titan entry [1] using a technique known as Shock Tube Informed Bias (STIB). This STIB [6] states that, in particle time, the normal component of velocity for an oblique shock has similarity with an incident shock and can be used to find shock tube conditions that are relevant to the backshell radiative heating. The relevant shot conditions were found using this method and a design trajectory for the Dragonfly capsule. Fifty-eight (58) shots were performed during this test series, named test 65, with velocities varying from 3 to 7 km/s and fill pressure mainly between 0.1 and 1.15 Torr. This paper will present the results and analysis of the Optical Emission Spectroscopy (OES) measurements made during this test series. Measurements were also performed using Laser Absorption Spectroscopy (LAS) of CN (Red) that has been discussed in a separate publication [7].

II. Experimental setup

The Electric Arc Shock Tube (EAST) facility has been described in detail in previous publications [8] [9]. The facility is composed of a 1.2 MJ, 40 kV capacitor bank that drives a 10.16 cm aluminum shock tube. The test gas consists of simulated Titan atmosphere – 97.8% N_2, 2.2% CH_4 by mole. A schematic of the EAST facility is presented in Figure 2. The test section of the facility is instrumented with four spectrometers looking at different wavelength regions: one in the Vacuum Ultraviolet (VUV), one in the UV/visible (Blue), one in the visible/near-infrared (Red) and one in the near infrared (IR) [8], see Figure 3. Radiation measurements in the UV/visible and in the visible/NIR are the most important as they include

most of the two main transitions of CN, namely CN Violet and Red. Therefore, the spectrometers were set to measure a spectrum from 220 to 1400 nm, with the VUV/Blue camera mainly measuring radiation from CN(Violet), while the Red/IR camera measure radiation from CN(Red). Measurements were also performed in the VUV (120-180 nm) for a few shots to confirm that no significant radiation was observed in this region. A summary of all shots performed with usable emission data is given in Appendix A.

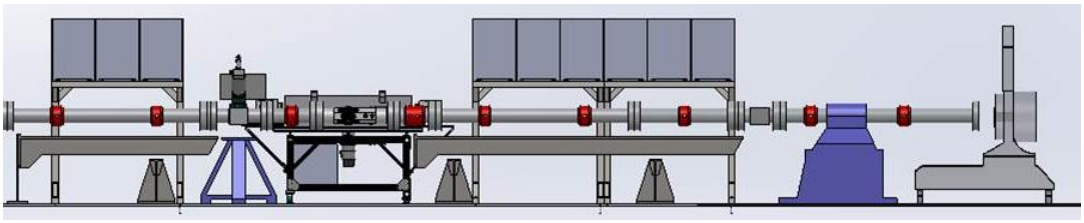

Figure 2: Schematic of the EAST facility.

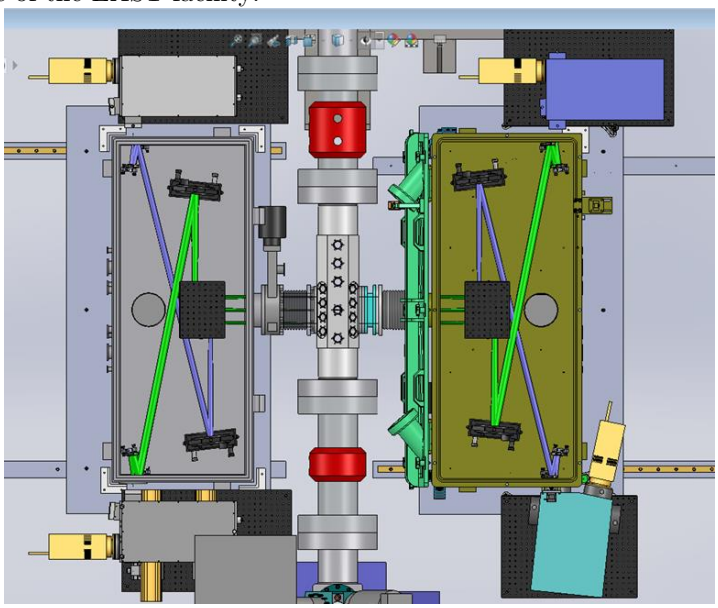

Figure 3. Instrumentation setup of the test section for OES.

III. Approach

An example of experimental data obtained from test 65 is presented in Figure 4. The data are spectrally and spatially resolved, giving a 3D map of radiance versus these two variables. Horizontal and vertical slices shown in Figure 4 represent the integrated radiance versus the spectral and the spatial variable, respectively. The radiation in the 340-430 nm range and measured by the VUV and Blue cameras is attributed to CN(Violet) while CN(Red) is measured by the Red and IR cameras in the 550-1400nm range. The radiative band close to the shock front at 335 nm corresponds to radiation of the NH (A-X) system [10]. This system is not observed for every shot, is always relatively weak (<5% of the total radiation), and decays rapidly. The band centered around 435 nm is attributed to the CH (A-X) system [11] which is even weaker and shorter lived than the NH band. Finally, the radiation measured in the 440-550 nm range corresponds to the C_2 swan bands and overlaps part of the CN Red system.

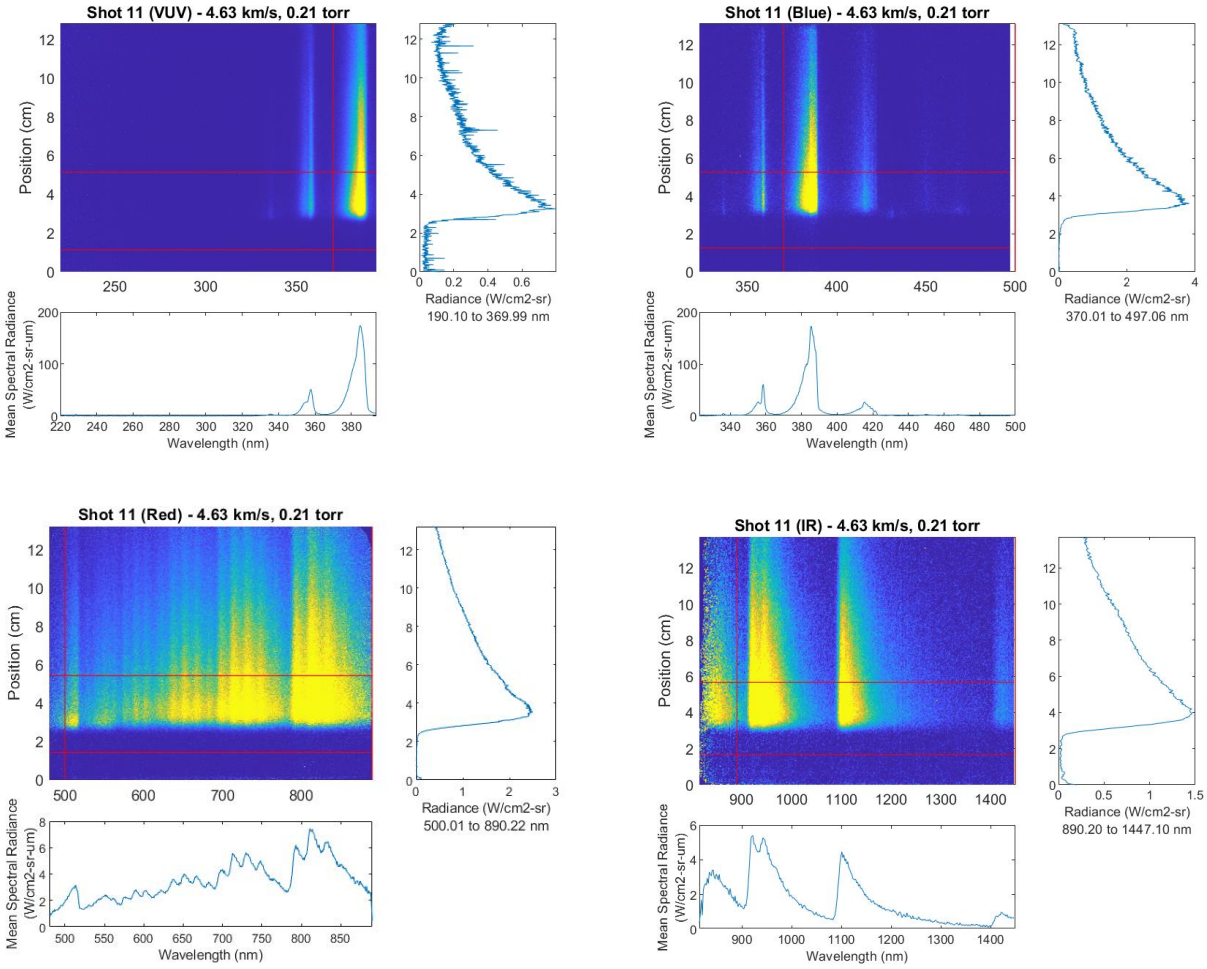

Figure 4: 3D spectral intensity maps obtained at 4.63 km/s and 0.21 Torr with all four cameras

In this work, both the spectral radiance and the total radiance are compared with computational predictions. The experimental shock front location is located using the trigger timing of the camera and the distance vs time relationship obtained from time of arrival measurements on the tube [8]. The measured radiance profiles are compared with NEQAIR [12] predictions based on equilibrium (chemical and thermal) conditions computed using CEA [13] [14] and CFD/NEQAIR predictions. CFD simulations were performed with DPLR [15] using the Gökcen kinetic model [16] by extracting the stagnation line from a flow around a 1-m sphere, at the freestream conditions equal to the test gas temperature and pressure and the measured velocity, in a similar way as done in Refs [17, 18]. The addition of the C_2N_2 molecule into the kinetic model was also studied as it was predicted to have a significant impact for some cases in Ref. [1]. The NEQAIR simulations are using the CN non-Boltzmann model implemented in NEQAIR v15.1, as CN electronic distribution was shown to be strongly non-Boltzmann for Titan entry [2]. In recent works [19], Clarke et al demonstrated that the time of flight for a simulation of a blunt body stagnation line can be different than the shock tube flow, due to the growth of the boundary layer in the post shock region, resulting in a slower core flow. The authors gave a spatial transformation to apply to the blunt body simulation to compare with

shock tube data [19]. This transformation was used in all results except where explicitly stated otherwise, and its effect will be discussed.

Finally, the measured radiance profiles are integrated over different wavelength ranges and binned over different distances from the shock front – the first being near the peak radiance region, similar to the previously defined nonequilibrium radiance metric [20, 21] and the second further away from the shock front to be more representative of the afterbody conditions. The STIB methodology is applied to the data at different distances from the shock front to determine the uncertainty at certain vehicle body locations.

IV. Optical Emission Spectroscopy results

A. Comparison between experiments and simulations

A comparison between different measured radiance profiles at fill pressure of 0.1, 0.21 and 0.3 Torr is presented in Figure 5. Only the radiance integrated over the Blue (420-490 nm) and Red (490-890 nm) cameras are presented, and are mainly dominated by radiation from CN(Violet) and CN(Red), respectively. For velocities above 4-4.5 km/s, the radiance profile has a similar shape as Figure 1, showing an increase in the early part of the shock before relaxing toward equilibrium. At lower velocities, there is no nonequilbrium peak in radiance observed, but only a slow increase, and it is unclear from this plot whether equilibrium is obtained.

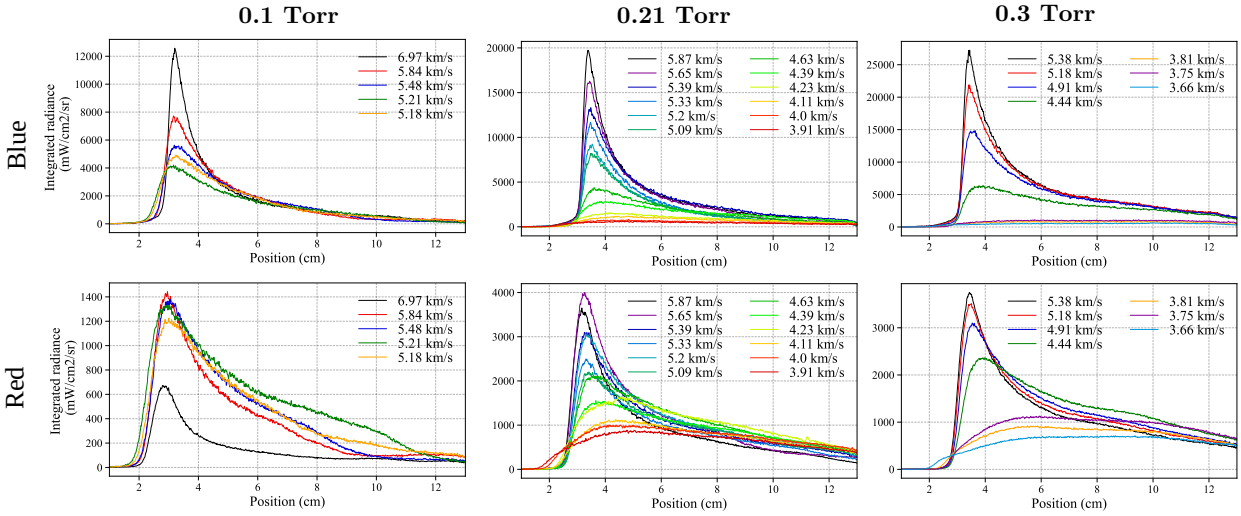

Figure 5: Comparison between measured radiance profiles for different shots at fill pressure of 0.1 (left), 0.21 (middle) and 0.3 (right) Torr integrated over the full wavelength range measured by the Blue (top) and Red (bottom) cameras

For more details, a comparison between the predicted and measured radiance profiles and spectra are presented in Figs 6 and 7. This was done for two shots representative of the higher and lower velocities. The time of flight transformation suggested in Ref. [19] was also applied and is compared to the results. The spectra correspond to spectra integrated over 1 cm, starting 5 cm from the shock front, to see the effect of the correction applied.

For the higher velocity case, the nonequilibrium radiance peak is overestimated for the VUV and Blue cameras, underestimated for the Red camera and is well predicted for the IR camera. For the Blue camera, dominated by the radiation of CN(Violet), the nonequilbrium peak is overstimated by about 50%. The Red camera nonequilibrium peak radiance is underestimated by about 20%, and while the radiation is dominated by the CN(Red) system, the misprediction of the nonequilibrium peak is mainly attributed to a misprediction of the C_2 Swan bands, which is also observed by the good prediction of the peak radiance in the IR camera. As will be discussed below, the relaxation towards equilibrium is also slower in the simulations compared to the measurements. The time of flight correction leads to an increase in the relaxation toward equilibrium, but remains slower than the measurements. The spectra comparisons indicate that the difference in the radiance profiles come from an overprediction of all systems, including CN(Violet) and CN(Red). The C_2 swan bands are also largely overpredicted as they are significant in the simulations, but very weak in the measurements (<5% of the total radiation). This is largely attributed to the lack of non-Boltzmann model for C_2 in NEQAIR.

For the lower velocity case, the simulations still predict a nonequilibrium peak radiance on the Blue and Red cameras, but not on the VUV and IR. Since the radiation measured by the VUV and IR camera is only coming from CN(Violet) and CN(Red), respectively, the nonequilibrium peak observed in the Blue and Red cameras is not attributed to CN, but mainly to a misprediction of the C_2 swan bands, and a slight overprediction of the NH bands for the Blue camera. Around 5 cm from the shock front, the simulations appear to predict a radiation level of CN Violet and CN Red above their equilibrium values, about 40% and 30% lower than predicted by CEA, respectively. while the measured radiation is about 30% and 10% higher than the DPLR prediction. For the lower velocity cases, the correction of the time-of-flight has little effect on the radiance profiles. For this shot, the radiance decrease around 8 cm from the shock front is attributed to the arrival of the contact front.

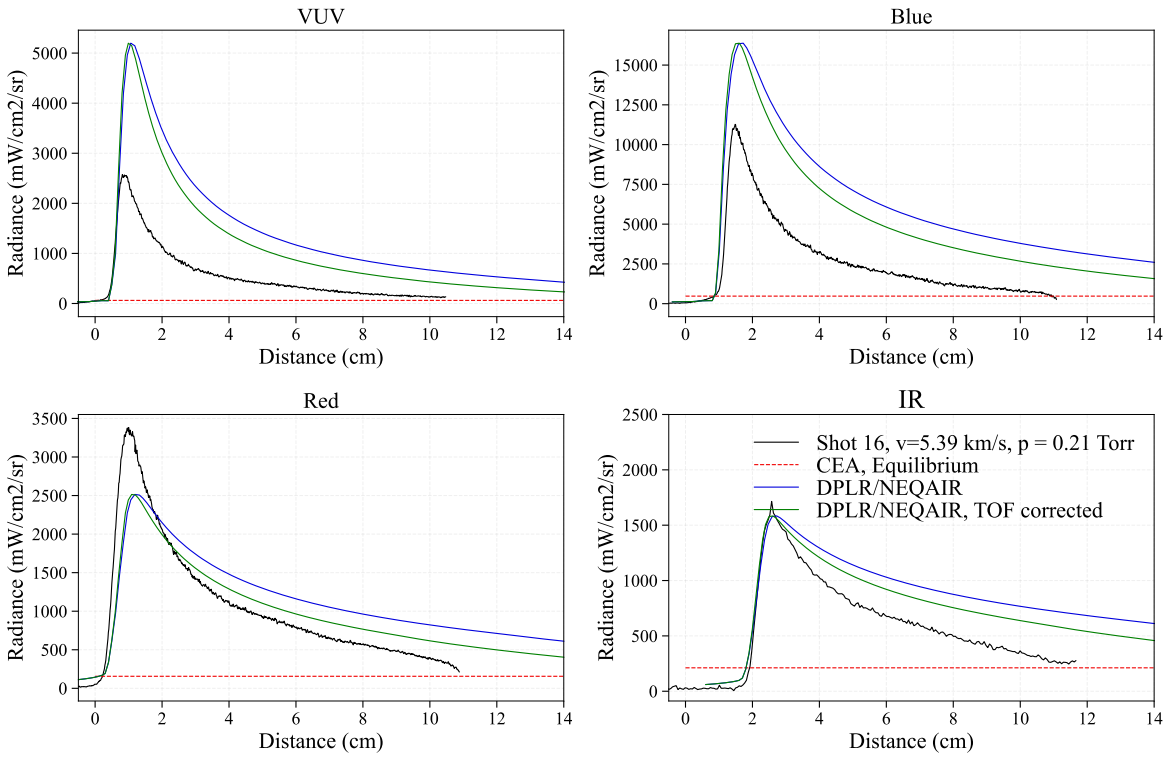

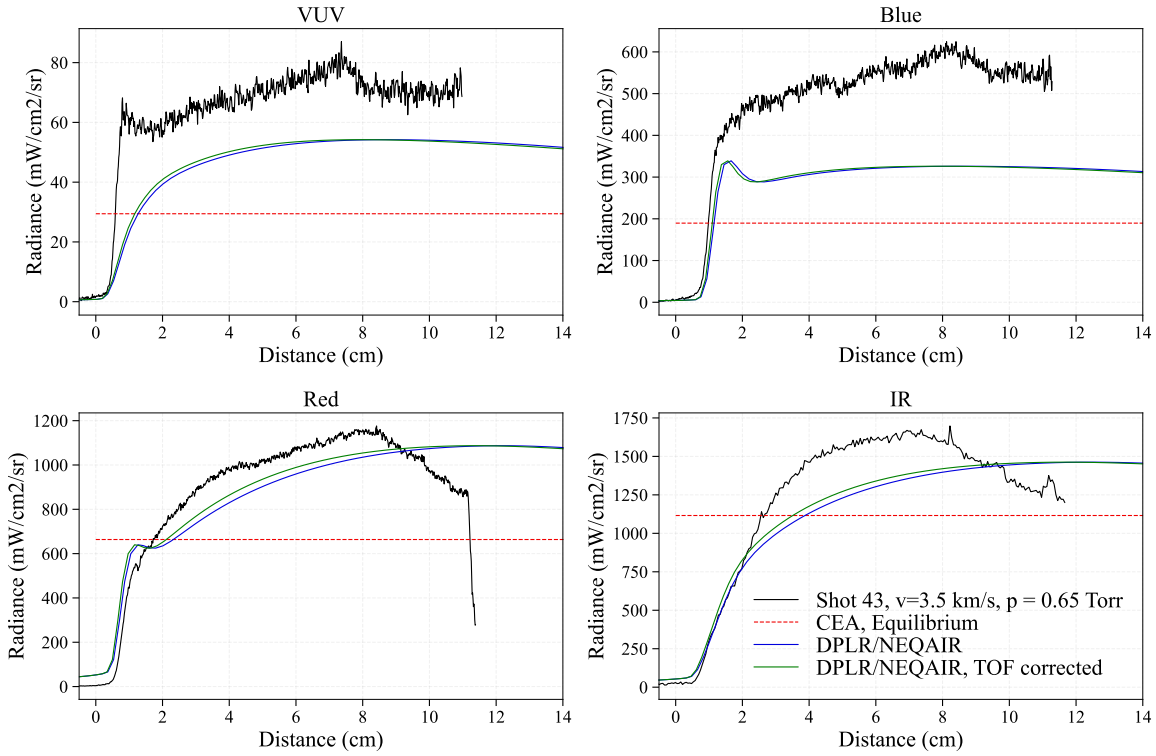

Figure 6: Comparison between measured (black) and computed integrated radiance profiles using CEA/NEQAIR or DPLR/NEQAIR predictions for two shots representative of higher and lower velocities of the test series. Results are shown both with and without the time-of-flight correction to the DPLR/NEQAIR results [19].

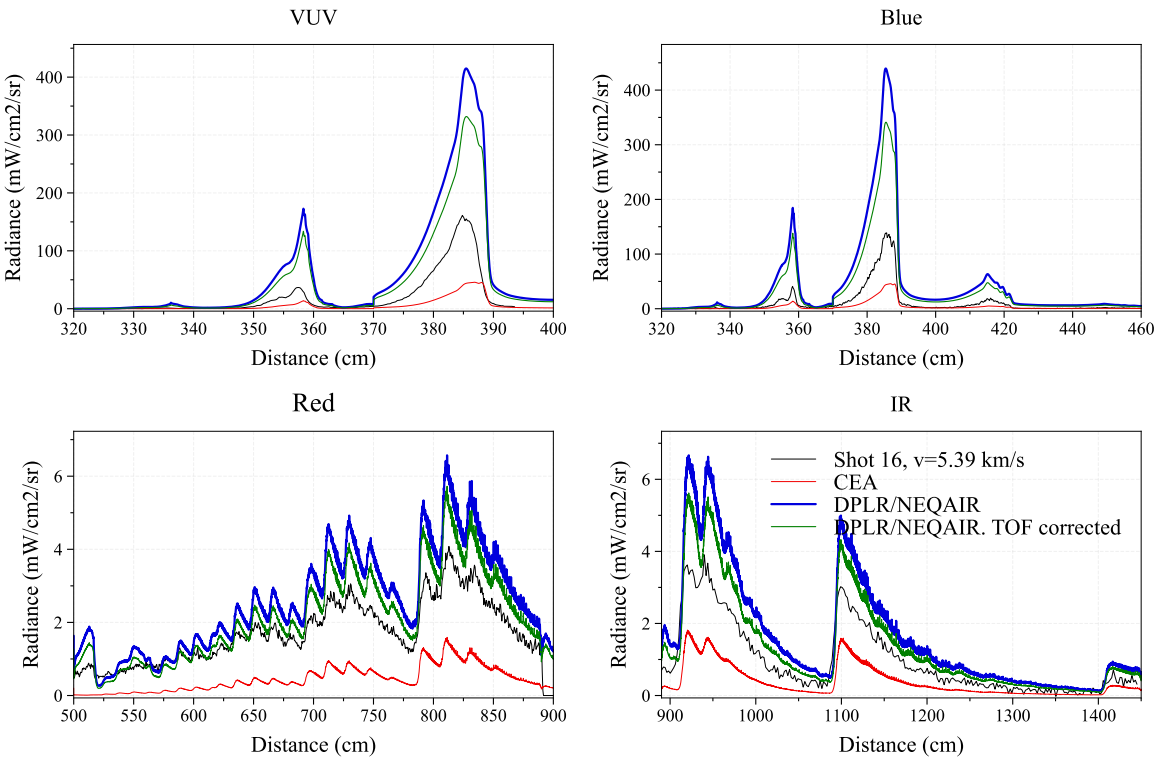

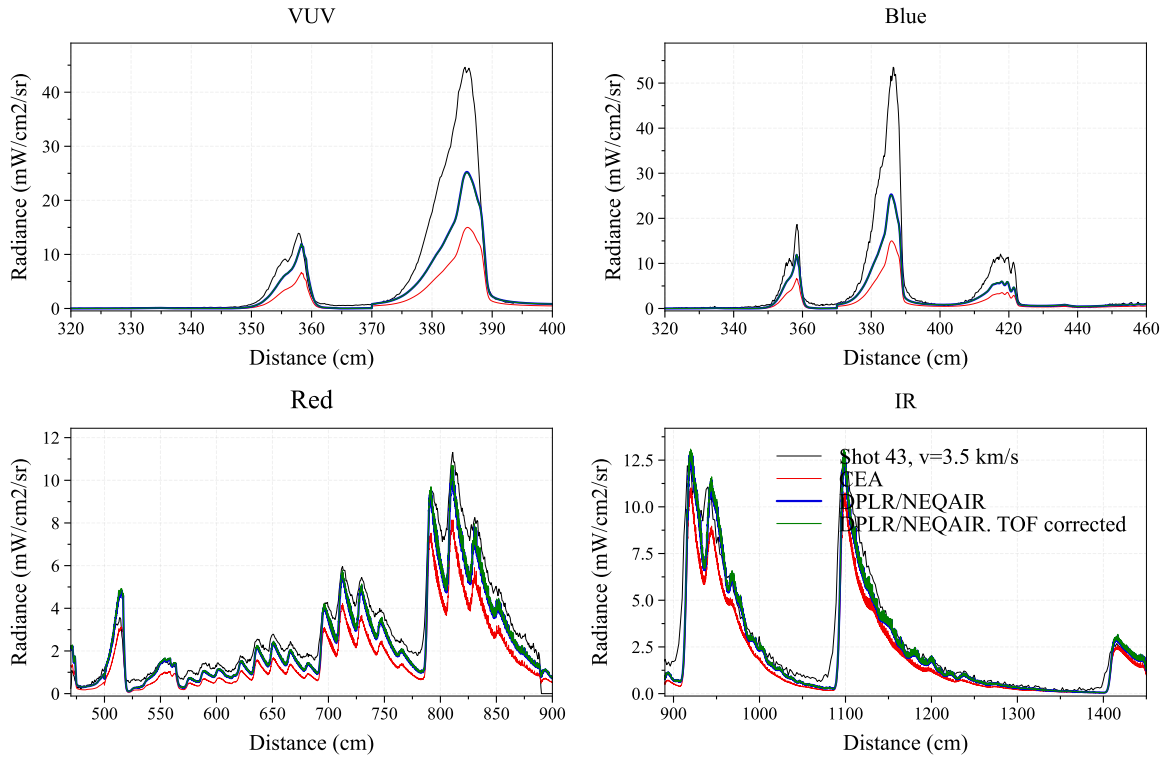

Figure 7: Comparison between measured (black) and computed spectra averaged from 5-6 cm behind the shock front using CEA/NEQAIR or DPLR/NEQAIR predictions for two shots representative of higher and lower velocities of the test series. Results are shown both with and without the time-of-flight correction to the DPLR/NEQAIR results [19]

To summarize the results from both measurements and simulations for all shots, the radiance was integrated over four wavelength ranges, representative of different radiative transitions: 330-430 nm for CN(Violet), 430-490 nm which is usually dominated by a continuum (originated from bound-free radiation) with sometimes radiation from C_2 Swan bands, 500-570 nm for C_2 Swan and 580-850 nm for CN(Red). The measured radiance is extracted from the Blue camera for the first two regions, while the other two are using data from the Red camera. The predicted radiance is computed using the DPLR/NEQAIR simulations including the time-of-flight correction, which is expected to represent a better comparison than without the correction [19]. Then, the radiance is averaged over 100 μs (in particle time), centered around the shock front in Figure 8. The particle velocity used is extracted from the DPLR simulations. The value obtained while averaging around the shock front location is similar to the nonequilibrium radiance metric defined in Refs [20, 21], which was using an average around ±2 cm, as the mean particle velocity is usually around 400 m/s. The use of particle time is motivated by the shock tube informed bias method results which are based on the time measured in the shock frame of reference. The errors between the measured and predicted radiance are also presented. CN(Violet) is the main source of measured radiation for all cases and is usually between 2 to 5 times stronger than CN(Red) while the C_2 Swan bands and the continuum are more than 10 times weaker than CN(Violet). The peak radiance increases for all bands with velocity. For CN(Violet), the peak radiance is underpredicted by about 60% at lower velocity, and the error increases with velocity to become overpredicted by about 150% at the largest velocity. Good agreement (within 20%) is observed in the 4-4.5 km/s range. For CN(Red), the peak radiance seems to be relatively well predicted, mostly

within ±30% from the measurements, with an underprediction at lower pressure, and an overprediction at higher pressure. The C_2 Swan bands are overpredicted at lower velocity and underpredicted at higher velocity and remain within ±50% from the measurements. The errors are also smaller at higher pressure, which is consistent with the lack of non-Boltzmann model in the simulations. Finally, the continuum radiation is well predicted below 4 km/s, and overpredicted to a maximum of 300% at larger velocity.

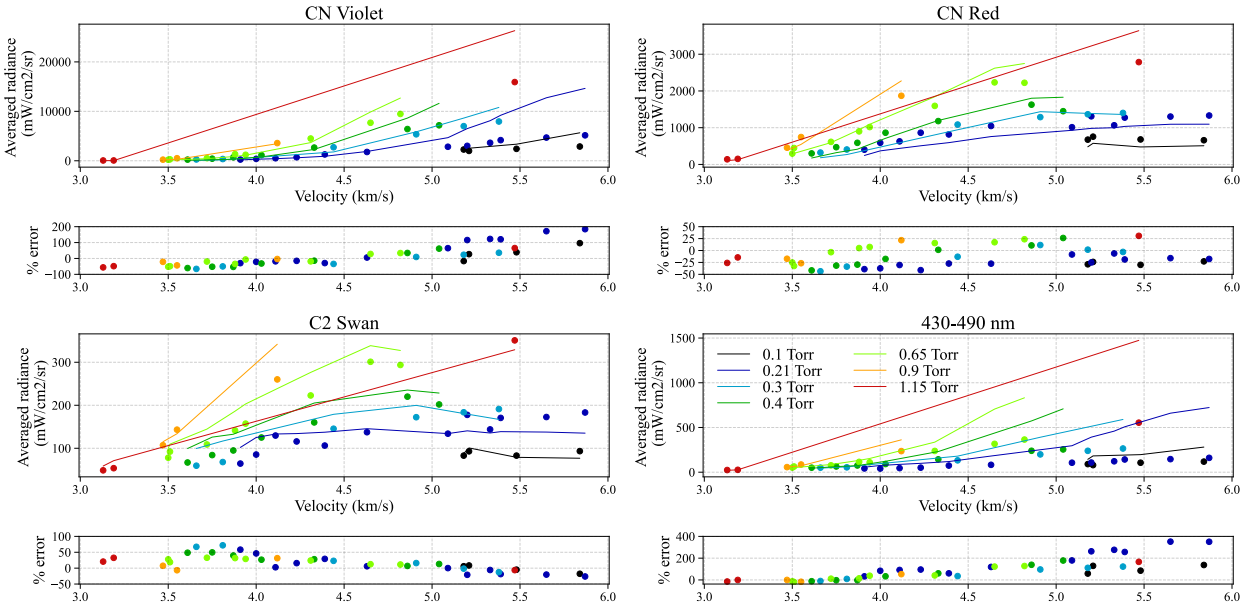

Figure 8: Comparison between measured (points) and computed (lines) peak radiance (±50 μs from the shock front) and errors for all fill pressure and all four wavelength ranges selected. Points and lines are color coded to show the pressure condition reported.

A similar comparison is made in Figure 9, where the radiance was averaged over 100-200 μs from the shock front, which should be more relevant for afterbody radiative heating. The measured radiation from CN(Violet) has decreased by about a factor of 2x. Below 5 km/s, the prediction accuracy is similar to that for the peak radiance, with the error increasing with velocity from -70 to +80%. Above 5 km/s, the agreement becomes worse, reaching up to 300% for the 0.21 Torr cases, and remain below 200% otherwise. The time-of-flight correction, applied in the results presented in Figure 9, is improving the agreement between measurements and predictions by a factor of about 1.4 above 5 km/s, but a large discrepancy still remains. For CN(Red), the disagreement is slightly worse, but remains mostly within ±50%, except for the 0.1 Torr cases, with an increase of the error above 4 km/s. The prediction of the C_2 Swan bands remain mainly within ±50% and the continuum prediction becomes worse but represent less than $1/20^{th}$ of the total measured radiance. In Figure 10, the contribution of each wavelength range is summed to show the total measured and computed radiance for every shot of the test series. The equilibrium radiance computed by CEA/NEQAIR is also shown for comparison. Both predicted and measured radiance show an increase with fill pressure, with the exception of the high velocity case at 1.15 Torr. The error seems to increase almost in a linear way from -50 to +200% from 3.5 to 6 km/s. This increase is due to a slower predicted relaxation towards equilibrium at larger velocities, as already observed in Figure 7.

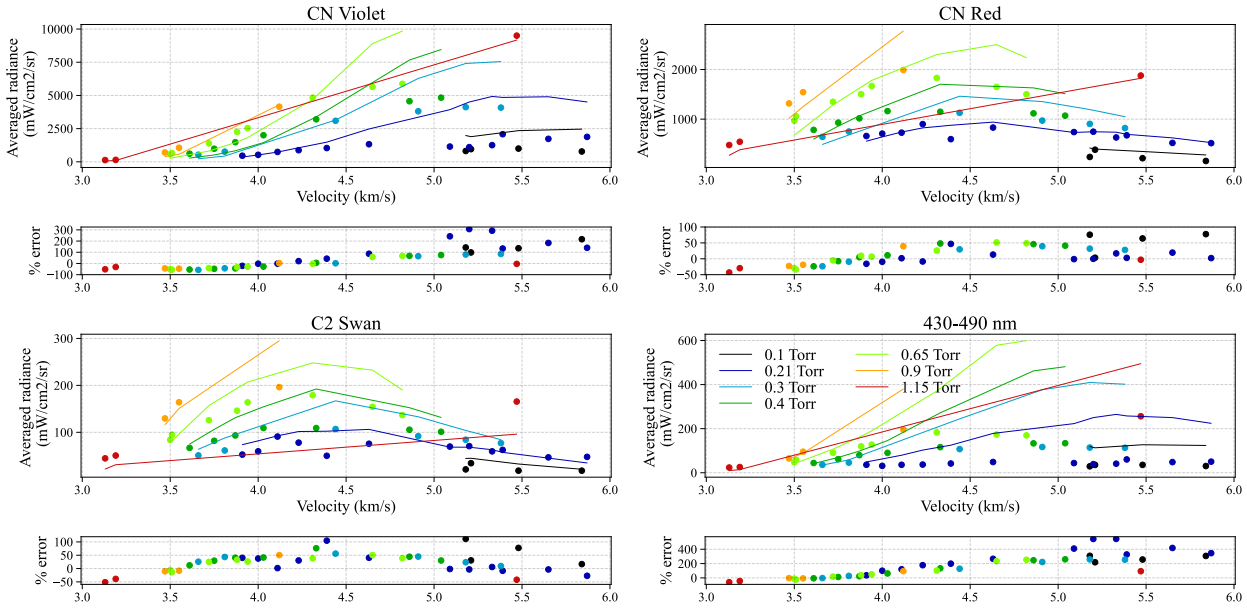

Figure 9: Comparison between measured (points) and computed (lines) radiance averaged over 100-200 µs from the shock front and errors for all fill pressure and all four wavelength ranges selected

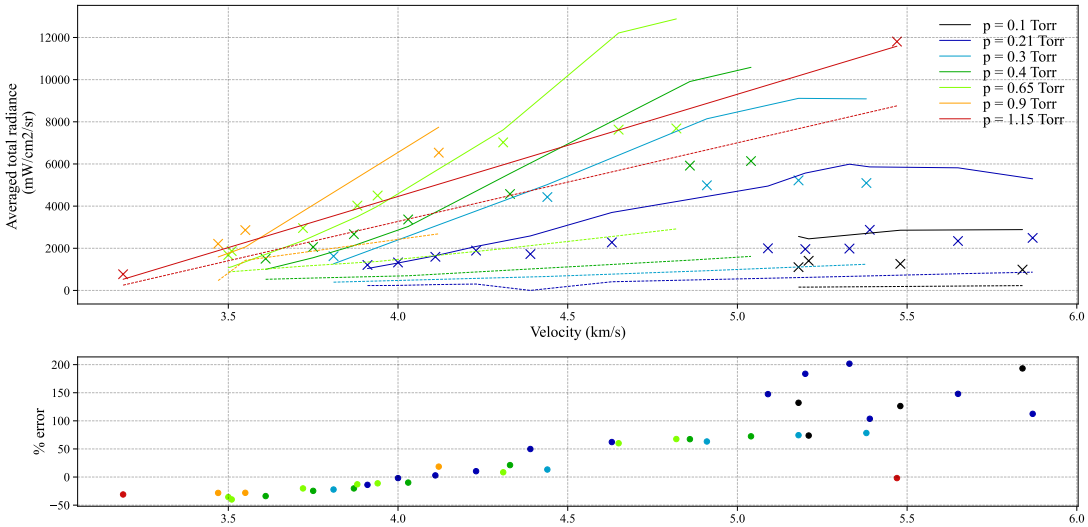

Figure 10: Comparison between the total measured (points) and computed (lines) radiance averaged over 100-200 µs from the shock front and errors for all fill pressures. The dashed lines represent the CEA equilibrium radiance.

The impact of the addition of the C_2N_2 molecule in the kinetic model was also studied. According to Ref. [1], C_2N_2 is generally present at velocities below 4 km/s, and will tend to decrease the density of CN, and therefore its radiation. C_2N_2 was therefore added into the DPLR kinetic model and compared to simulations without it. No significant impact on radiation was observed near the shock front. At lower velocity, C_2N_2 slightly decreases the total predicted radiation at distances further from the shock front, with increasing impact at longer distance. As an example, a comparison between the total radiation predicted with and without C_2N_2 averaged between 100 and 200 µs from the shock front is presented in Figure 11. The difference between the two models is negligible (<1%) above 4 km/s. Below 4 km/s, the model with

C_2N_2 predicts a slightly lower radiation, with a maximum difference of 4%. The impact of C_2N_2 may be larger at a surface point further along the backshell where radiation may come from times larger than 150 μs. This regime can explain the 15% difference reported in Ref. [1]. As the radiation is underpredicted below 4 km/s, as shown in Figure 10, the addition of C_2N_2 will increase the discrepancy with the measurements. Therefore, simulations without C_2N_2 are employed in the rest of this paper.

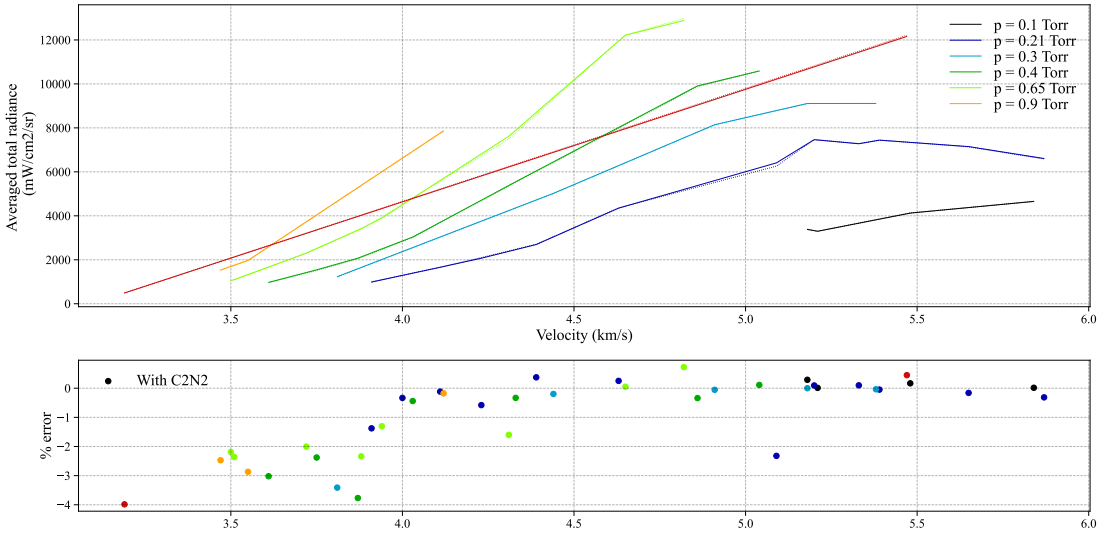

Figure 11: Comparison between the total radiance computed without (solid) or with (dashed) the addition of C_2N_2 averaged over 100-200 μs from the shock front and errors for all fill pressures.

As discussed above, Fig. 7 suggested that the predicted chemistry is slower than the measurement, leading to a larger predicted relaxation time and higher predicted radiances in Fig. 10. This is demonstrated quantitatively by fitting the radiance profiles with an exponential curve trending to the equilibrium value obtained by CEA and extracting the characteristic relaxation time to equilibrium. Both measured and predicted profiles were fit the same way to ensure consistency in the comparison. A different relaxation time was obtained for CN Violet and CN Red. Results for all fill pressures are presented in Figure 12, with trendlines added to guide the eye. Despite some scatter in the data, a clear trend is visible. For CN Violet, the predicted relaxation time is higher than measured, by a factor 1.5 to 3.5, with the discrepancy increasing at lower velocity. The predicted relaxation time decreases with increasing fill pressure. The relaxation times obtained by fitting the radiance profiles of CN Red are larger than those obtained from CN Violet for both the simulations and the measurements. This difference increases at lower velocity and remains below a factor of about 1.5. The discrepancy between predictions and measurements remains about the same using either CN Violet or CN Red.

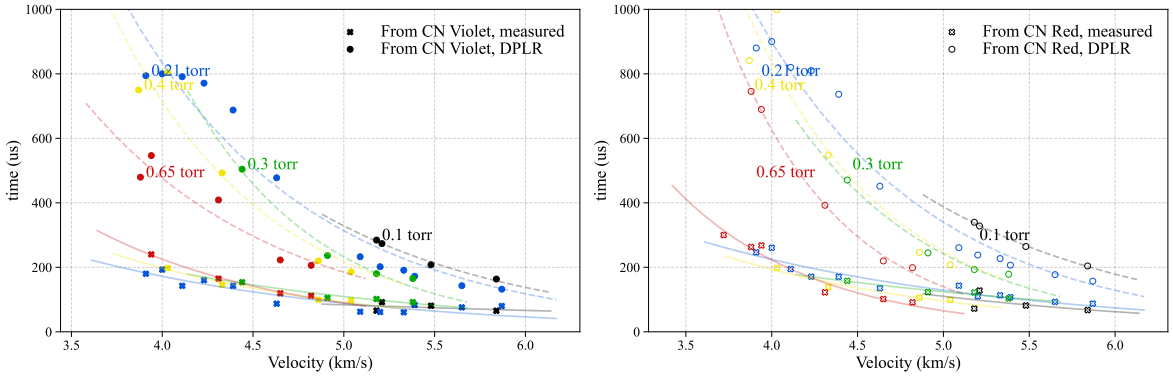

Figure 12: Relaxation time obtained by fitting the measured (cross) and predicted (circle) radiation profiles of CN Violet (left) and CN Red (right). The solid and dashed lines are provided to represent the trends of the measured and predicted relaxation times.

B. Estimation of the error for the backshell radiative heat flux

One of the primary goals of this test series is to validate the models used for radiative heating on the backshell for Titan entry using the shock tube informed bias and flowfield property binning methods [22, 1]. The results obtained in this test series can be used to provide a preliminary estimate of the total predicted error of the radiation during the Dragonfly capsule entry. The t=231s point in the trajectory, which corresponds to a fill pressure of 0.4 Torr in the EAST facility, is chosen as an example. The results of the STIB method are shown in Figure 13. The 2D map of the normal shock velocity, which corresponds to the shock velocity in EAST, is presented versus location in the pitch plane of the flowfield. The contribution to the wall radiative heat flux at four different surface points (marked a-d on the backshell image) are displayed as histograms versus normal shock velocity and particle time in the shock frame of reference. For point A just before the shoulder, most of the wall radiative heat flux comes from gas shocked at 5.1 km/s after travelling 10 μs to 1 ms. Looking at the point B just after the shoulder, the particle time and velocity range of interest is about the same with some contribution from gas shocked between 4 and 5 km/s being observed. At point C, the shocked gas velocity of interest is decreased to 3.5 to 5 km/s and particle time range increases to 50 μs to 1 ms. Finally at point D near the back of the capsule, the velocity range of interest decreases to 3 to 4.5 km/s and the particle increases to 100 μs to 2 ms.

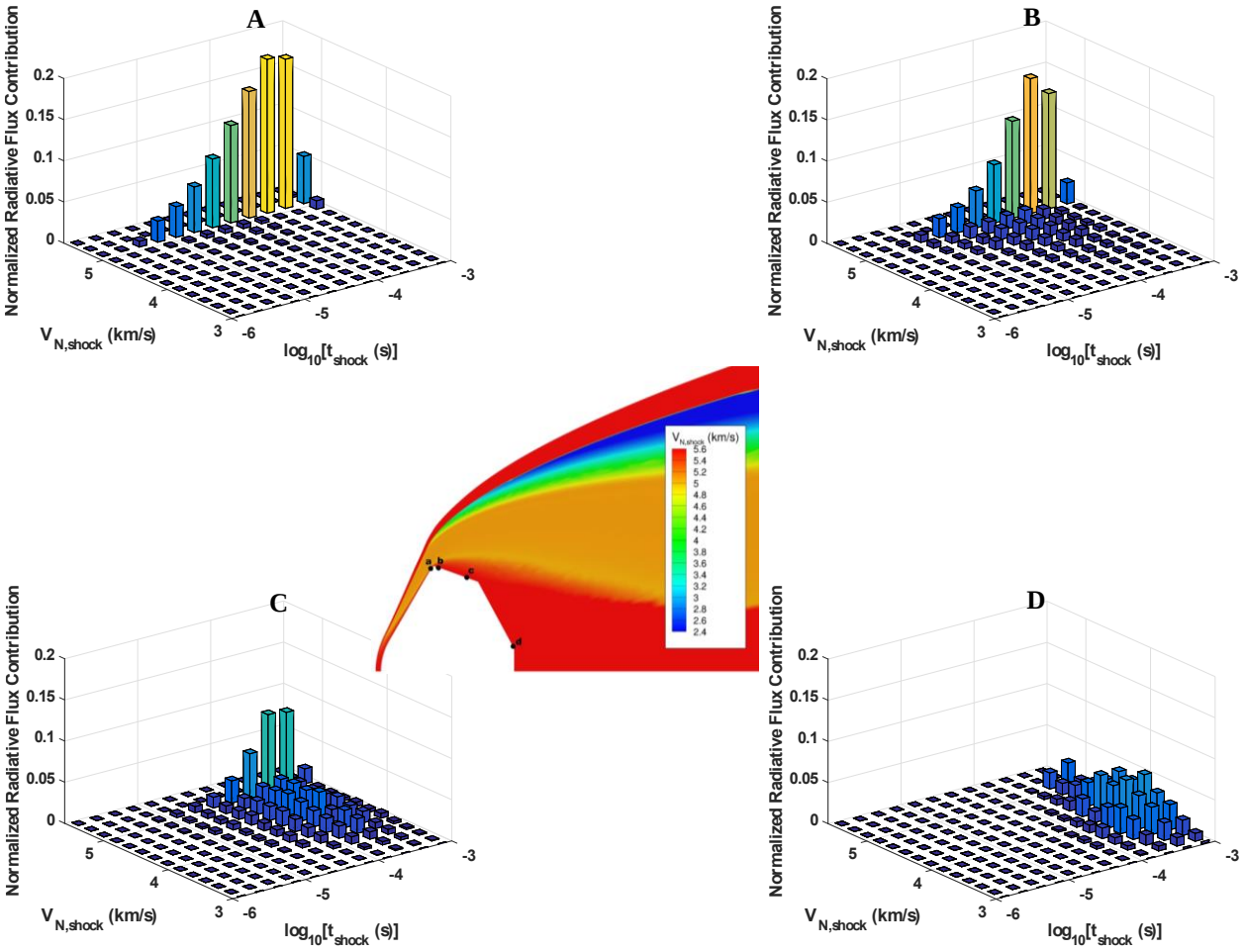

Figure 13: Radiative heating bin distributions for 4 different surface point of the DragonFly capsule at a freestream pressure of 0.4 Torr (t=231 s). The locations of those points are shown in the 2D map of the normal shock velocity presented in the center for that specific trajectory point.

For most of the shots studied in the EAST facility, no data was collected after about 200-250 μs from the shock front. To obtain an estimated error at larger time, the measured radiance profiles were extrapolated using an exponential curve, in a similar way as used to obtain the relaxation times in Figure 12, in the 420-1400 nm range. At a fill pressure of 0.4 Torr, there are 7 shots with usable data, ranging from 3.61 to 5.04 km/s. However, the shots at velocity below 4 km/s do not show an exponential decrease and could not be extrapolated. For those shots, the error was assumed constant at larger time. To extrapolate the comparison at higher and lower velocities, the measured errors as a function of velocity are fit using a linear curve, which seems a reasonable assumption based on Figures 8-10. These two approaches are used to generate a 2D map of the errors between measured and predicted radiance as a function of velocity and particle time, presented in Figure 14. The conditions of interest representing 90% of the total wall radiative heat flux, in terms of shock velocity and particle time, for the four surface points defined previously are plotted as contours in Figure 14. In the ranges considered, the error is mostly between -150 to +150 % and is maximum at around 500 μs, just outside the edge of the measured range. After about 2 ms, the error

approaches zero for velocities above 4 km/s, indicating that equilibrium has been reached in both measured and predicted radiance profiles. The conditions relevant for the surface points A and B have significant overlap with the measured interval, while there is less overlap for point C, and point D will rely mainly on extrapolated data. Nevertheless, by integrating the histograms of Fig 13 across the contours of Fig 14, we can estimate the total estimated error at the four surface locations. Results are presented in Table 1. The largest error is near the shoulder, with an overprediction of 102% (i.e. 2x high). Just after the shoulder, the error is at 92%. Further away from the shoulder, the error decreases to 65 and 14% on points C and D, respectively. The reduced error is a consequence of the larger particle times considered, allowing the gas to relax toward equilibrium where the uncertainty is assumed to be zero, and the underprediction of the radiative heat flux at lower velocities, which is clearly seen on Figure 14. The reported error represents only a preliminary estimate of the total error encountered by the Dragonfly afterbody, and is not aimed to be used for the design of the heatshield, as it requires further analysis.

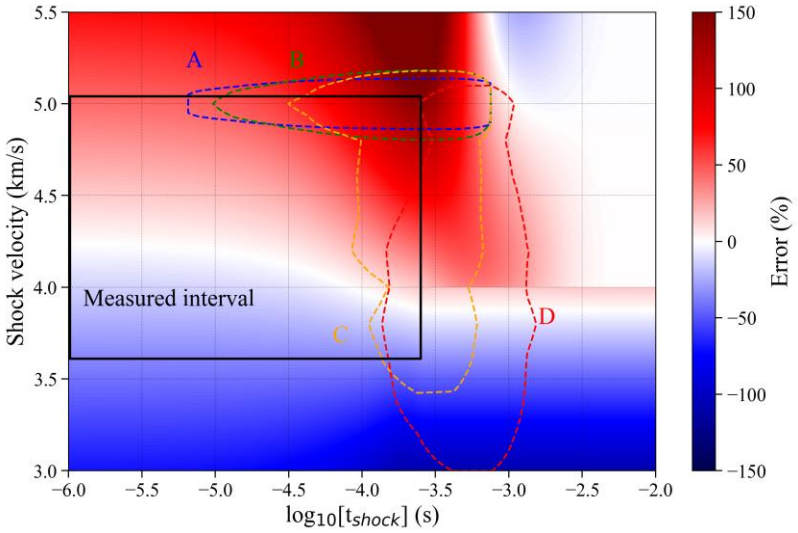

Figure 14: 2D error map between predicted and measured radiance from 420 to 1400 nm. The black rectangle represents the measured ranges, and points outside of it were extrapolated. The contour of the conditions relevant for the surface points A, B, C and D are also shown.

Table 1: Estimated error on the predicted wall radiative heat flux at the four surface points considered

Surface point	A	B	C	D
Estimated error	**+102%**	**+92%**	**+65%**	**+14%**

C. Temperature and number densities comparison

Finally, the measured radiance was binned over 0.5/1 cm intervals and fit to obtain post-shock number densities and temperatures. The binning interval is chosen as a compromise between having both good signal-to-noise ratio and spatial resolution. The fits are performed using the NEQAIR radiation code in a similar way as presented in Refs [26] [27]. Both the spectra obtained from the Blue and Red cameras were fit, and only the contribution of CN Violet and CN Red were considered. The reported uncertainties in the emission data represent both systematic and random errors. The systematic error was estimated using the error of the fit parameters. For the random errors, a random and gaussian artificial noise of amplitude equal

to the measured noise was added to each spectrum. These new created spectra were then fit again. This was performed 10 times and an error equal to twice the standard deviation of the results was added to the error on the fit parameters. The total reported errors still do not take into account uncertainties coming from the construction of the radiation model. The reported center value for the temperatures and number densities correspond to the mean of all fitted spectra. The data obtained from OES are compared with the TDLAS measurements performed and presented in Ref. [7] and simulations from DPLR and CEA. Temperature results are presented in Figure 15 for five different shots. Both the translational-rotational and the vibrational-electronic temperatures are given for the DPLR simulations, while the experimental data only contain a single (mean) temperature. At velocities below 4 km/s, the OES temperatures appear to be larger than the predictions, typically by 10 to 15%. At larger velocities, a good agreement is observed between the measurements and the predictions, with a predicted temperature lying inside the uncertainties at 4.86 km/s, while, at 5.65 km/s, a difference below 4% is observed between the measurements and the predictions. The temperatures obtained using the Red camera appear to be lower than those obtained from the Blue camera early in the shock front. The difference between the temperatures while fitting the radiance profiles on both cameras could indicate that the fitted temperature from the Red camera is more sensitive to the vibrational temperature than the rotational one. A good agreement is observed between the two measurements after 1-1.5 cm from the shock front. Also included are the translational temperatures that are obtained with TDLAS for three of the shots [6]. These results generally overlap the error bars of the OES measurement. The discrepancy below 4 km/s further away from the shock front could be explained by shock deceleration effects, which will tend to increase the predicted temperature as previously observed in Ref. [23]..

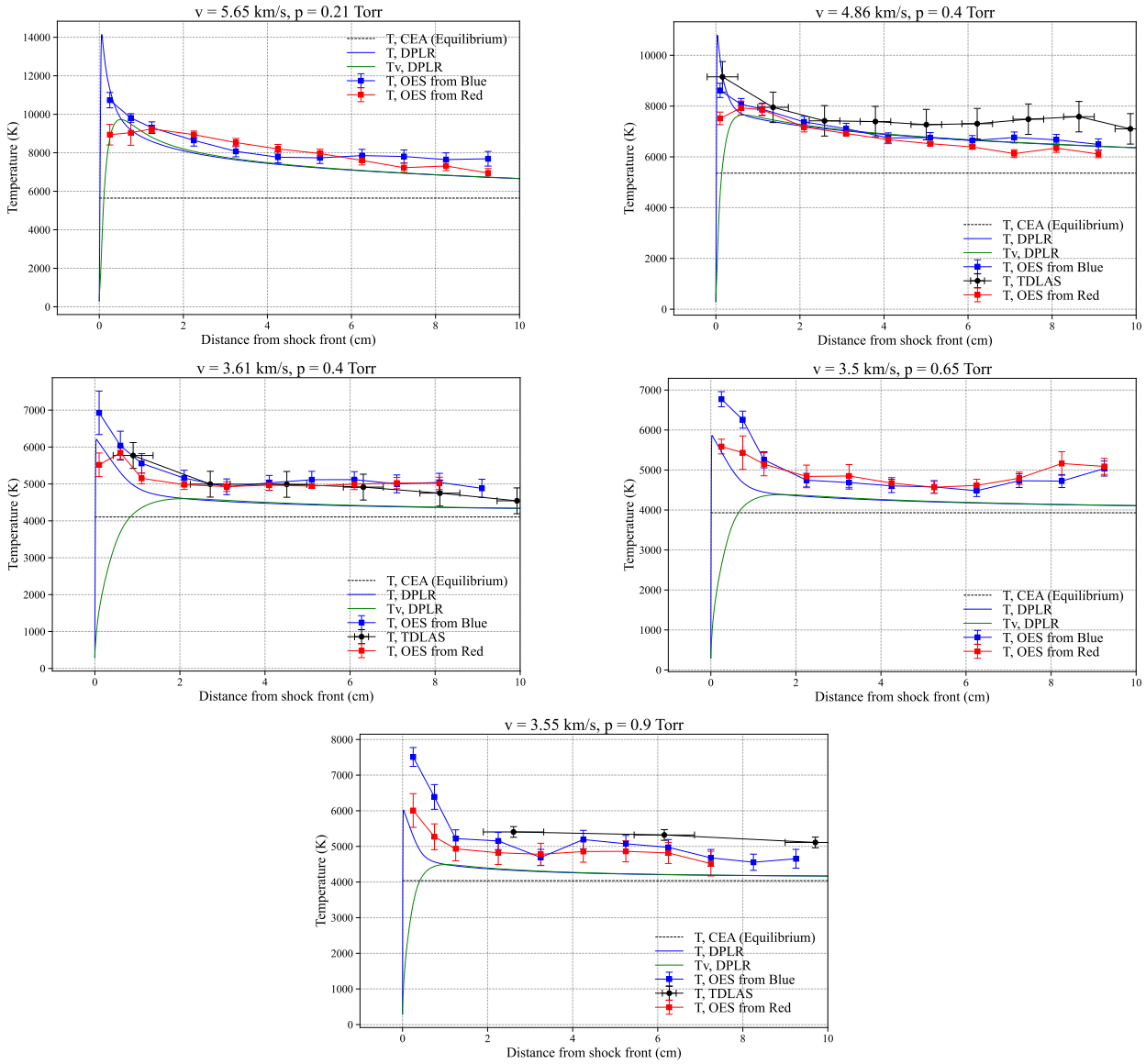

Figure 15: Comparison between measured temperatures inferred from OES (square) and TDLAS (circle) and predicted temperatures from DPLR (solid line) and CEA (dashed line).

Comparison between measured and predicted CN number densities are presented in Figure 16. The spectra obtained by OES were fit by adjusting the density of the upper state of the CN Violet and CN Red transitions, to yield a direct measurement of the density of CN(B) and CN(A), respectively. A potential absorption of the lower state CN(X) was also taken into account by adjusting the total number density of CN. The DPLR/NEQAIR simulations presented through the paper are using a Non-Boltzmann (NB) model for CN and the resulting densities of the A and B states are presented, with the addition of the Boltzmann densities for comparison. Finally, CN(X) density from the TDLAS measurements of Ref.[6] are included for three of the tests.

For the low velocity cases (<4 km/s), the density of CN(X) measured by TDLAS is underpredicted early in shock. The measurements show an overshoot of equilibrium, followed by decay, while the predictions

increase steadily and exceed equilibrium. These observations are consistent with the temperature trends in Fig. 14. These differences could be a combination of an artifact due to the use of the stagnation line of a blunt body as a simulation, and the impact of shock deceleration in the experiment [24]. This latter point could be resolved by using a better 1D shot solver such as the one presented in Ref. [23]. The predicted density of CN(A) is found to be relatively close to Boltzmann conditions and the measured densities are in good agreement with the predictions, as expected from the relatively low errors previously observed in Figs 8 and 9. The measured density of CN(B) is close to the Boltzmann condition and is underpredicted by the non-Boltzmann model by about 40%, except at larger pressure where a good agreement is observed. CN(A) and CN(B) number densities also reach their corresponding equilibrium values before the end of the measurement region and equilibrate sooner with increasing pressure, which is consistent with the results of Figure 12.

For the larger velocity case, the density of CN(X) is underpredicted by about 20-30%. The measured density of CN(A) is well predicted close to the shock front and becomes underpredicted further away, which is consistent with the radiation measurements. The measured density of CN(A) reaches its equilibrium value after 9 cm but may keep going down at longer distance as the measured temperature and ground state density are still far from equilibrium.. CN(B) is always predicted to diverge significantly from Boltzmann conditions and is overpredicting the measured density with a discrepancy increasing at larger distance from the shock front.

Based on these comparisons, the main issue in the predictions seems to come from the non-Boltzmann model used, as the temperature are relatively well predicted. The NB model predicts correctly the density of CN(A) early in the shock front, but then predicts a slower relaxation at higher velocities. For CN(B), the non-Boltzmann model has too much impact on the resulting density at lower velocity, and too little impact at higher velocity.

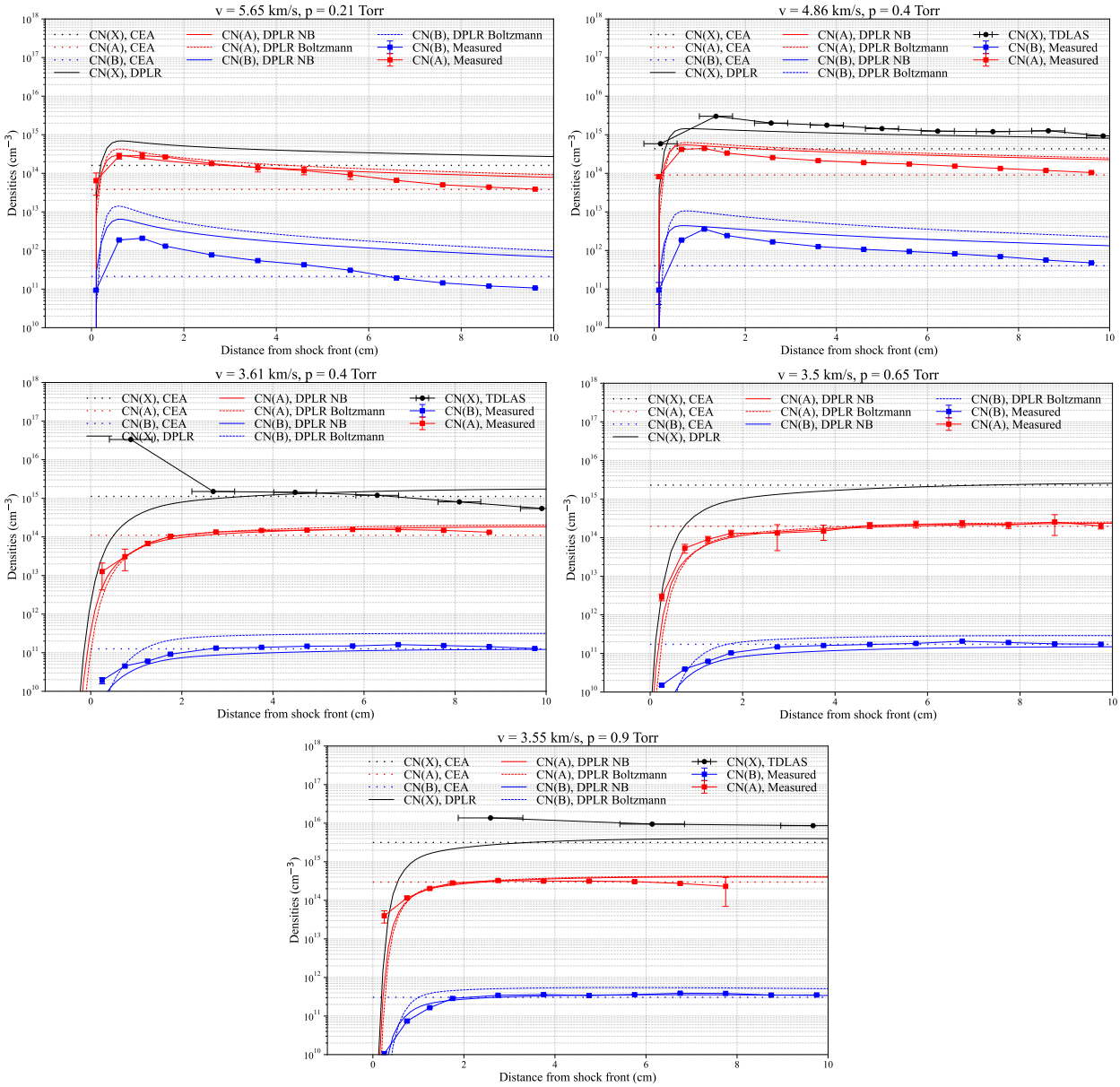

Figure 16: Comparison between measured CN number densities inferred from OES (square) and TDLAS (circle) measurements and predicted temperatures from DPLR (solid line) and CEA (dashed line).

V. Conclusions

A test series was performed in the EAST facility aiming to reproduce the backshell condition that the Dragonfly capsule will encounter during its entry into Titan's atmosphere. OES measurements were performed and compared to CFD simulations. A non-Boltzmann model of CN was also used. Both the peak radiance, and the decrease of the radiance later in the shock are mispredicted by the model. The CN Red was relatively well predicted, remaining within ±50% of the prediction at all times measured. Therefore, the main source of discrepancy comes from the misprediction of the CN Violet radiation, leading to an uncertainty on the total radiation starting from -40 to +100% difference for the peak radiance, to -50 to

200% difference 150 μs (~7 cm) from the shock front. The C_2 swan bands were relatively well predicted, within ±50%, and the differences could come from the lack of non-Boltzmann model. Given that the measured radiation of C_2 was always found to be below 6% of the total radiation, such NB model may not be needed for C_2.

A preliminary estimate of the total error between measurements and predictions was given at four different locations on the backshell for one time of the Dragonfly trajectory, which all yield overprediction on the wall radiative heat flux. The maximum discrepancy was found to be around the shoulder of the capsule, around 100%, decreasing to 14% on the back of the capsule. The error was always conservative at this point in time. At later times in the trajectory, where the velocity is slower, the error may change to be non-conservative.

Comparison between inferred temperature and number density measured by OES and TDLAS and simulations were also performed. Temperatures were found to be in good agreement at larger velocities, and underpredicted by about 500K at lower velocities. This latter discrepancy may be attributed to shock deceleration effects and may be corrected by using a better 1D shot solver, as previously performed in Ref. [23]. A good agreement between the temperatures measured by both OES and TDLAS was found for all shots presented. For velocity below 4 km/s, the measured number density of CN(X) was found to be mispredicted by the simulations, which may also be due to shock deceleration effects. The number density of CN(A) was found to be predicted close to Boltzmann distribution, and a good agreement with the measurements was found at lower velocity, and early in the shock at larger velocities. For CN(B), the simulations underpredicted the measurements by about 40% at lower velocity and pressure, with a good agreement observed at larger pressure. At larger velocities, the CN(B) number densities is underpredicted while a good agreement between the predicted and measured number density of CN(X) is observed. Based on these results, the non-Boltzmann model of CN as implemented in DPLR/NEQAIR should be improved in order to decrease the observed discrepancy between simulations and measurements. Improving that model seems to be the key for a better prediction of the radiation encountered by a capsule entering Titan's atmosphere and may be the focus of future research.

Acknowledgments

Augustin Tibere-Inglesse's research was supported by an appointment to the NASA Postdoctoral Program at the NASA Ames Research Center, administered by Oak Ridge Associated Universities under contract with NASA. Brett Cruden is supported by NASA contract NNA15BB15C to Analytical Mechanical Associates, Inc. This work was supported by the Entry Systems Modeling project.

References

[1] C. O. Johnston, T. K. West and A. M. Brandis, "Features of Afterbody Radiative Heating for Titan Entry," *AIAA Aviation 2019 Forum,* 2019.

[2] A. Brandis and B. A. Cruden, "Titan Atmospheric Entry Radiative Heating," *47th AIAA Thermophysics Conference, AIAA Aviation Forum,* no. 2017-4534, 2017.

[3] D. Bose, M. J. Wright, D. W. Bogdanoff, G. A. Raiche and G. A. Allen, "Modeling and Experimental Assessment of CN Radiation Behind a Strong Shock Wave," *Journal of Thermophysics and Heat Transfer,* vol. 20, no. 2, pp. 220-230, 2006.

[4] C. M. Jacobs, T. J. McIntyre, R. G. Morgan, A. M. Brandis and C. O. Laux, "Radiative Heat Transfer Measurements in Low-Density Titan Atmospheres," *Journal of Thermophysics and Heat Transfer,* vol. 29, no. 4, pp. 835-844, 2015.

[5] A. M. Brandis, R. G. Morgan, T. J. McIntyre and P. A. Jacobs, "Nonequilibrium Radiation Intensity Measurements in Simulated Titan Atmospheres," *Journal of Thermophysics and Heat Transfer,* vol. 24, no. 2, pp. 291-300, 2010.

[6] C. O. Johnston, "Evaluating Shock-Tube Informed Biases for Shock-Layer Radiative Heating Simulations," *Journal of Thermophysics and Heat Transfer,* vol. 35, no. 2, pp. 349-361, 2020.

[7] E. Chang, J. Streicher, C. Strand, R. Hanson and B. M. Cruden, "Laser Absorption Spectroscopy Measurements of Post-Shock Non-Equilibrium Species in the NASA Ames Electric Arc Shock Tube," *2023 AIAA Scitech Forum,* 2023.

[8] B. Cruden, R. Martinez, J. Grinstead and J. Olejniczak, "Simultaneous Vacuum-Ultraviolet Through Near-IR Absolute Radiation Measurement with Spatiotemporal Resolution in An Electric Arc Shock Tube," *41st AIAA Thermophysics Conference,* Vols. AIAA 2009-4240, AIAA, San Antonio, TX, 2009.

[9] S. P. Sharma and C. Park, "Operating Characteristics of a 60- and 10-cm Electric Arc-Driven Shock Tube-Part 11: The Driven Section," *Journal of Thermophysics and Heat Transfer,* vol. 4, no. 3, pp. 266-272, 1990.

[10] W. H. Smith and H. S. Liszt, "Frank-Condon factors and absolute oscillator strengths for NH, SiH, S2 and SO," *Journal of Quantitative Spectroscopy and Radiative Transfer,* vol. 11, no. 1, pp. 1-45, 1971.

[11] A. Kalemos, A. Mavridis and A. Metropoulos, "An accurate description of the ground and excited states of CH," *J. Chem. Phys,* vol. 111, no. 21, pp. 9536-9548, 1999.

[12] E. Whiting, C. Park, L. Yen, J. Arnold and J. Paterson, "NEQAIR96,Nonequilibrium and Equilibrium Radiative Transport and Spectra Program: User's Manual," Technical Report NASA RP-1389, Ames Research Center, Moffett Field, 1996.

[13] S. Gordon and B. McBride, "Computer program for calculation of complex chemical equilibrium compositions and applications. Part 1: Analysis," NASA RP-1311, 1994.

[14] B. J. McBride and S. Gordon, "Computer Program for Calculation of Complex Chemical Equilibrium Compositions and Applications II. User's Manual and Program Description," *NASA RP-1311-P2,* June 1996.

[15] M. J. Wright and D. Bose, "Data-Parallel Line Relaxation Method for the Navier-Stokes Equations," *AIAA Journal,* vol. 36, no. 9, pp. 1603-1609, 1998.

[16] T. Gökcen, "N2-CH4-Ar Chemical Kinetic Model for Simulations of Atmospheric Entry to Titan," *Journal of Thermophysics and Heat Transfer,* vol. 21, no. 1, pp. 9-18, 2007.

[17] B. A. Cruden, A. M. Brandis and D. K. Prabhu, "Measurement and Characterization of Mid-wave Infrared Radiation in CO2 Shocks," *11th AIAA/ASME Joint Thermophysics and Heat Transfer Conference,* Vols. AIAA 2014-2962, 2014.

[18] B. A. Cruden, A. M. Brandis and D. K. Prabhu, "Compositional Dependence of Radiance in CO2/N2/Ar Systems," *44th AIAA Thermophysics Conference,* no. AIAA 2013-2502, 2013.

[19] J. Clarke, M. McGilvray and L. Di Mare, "Numerical simulation of a shock tube in thermochemical non-equilibrium," in *AIAA SciTech conference,* 2023.

[20] A. M. Brandis, C. O. Johnston, B. A. Cruden and D. K. Prabhu, "Investigation of Nonequilibrium Radiation for Mars Entry," *51st AIAA Aerospace Sciences Meeting including the New Horizons Forum and Aerospace Exposition, Aerospace Sciences Meetings,* no. AIAA 2013-1055, 2013.

[21] B. A. Cruden and A. M. Brandis, "Measurement and Prediction of Radiative Non-equilibrium for Air Shocks Between 7-9 km/s," *American Institute of Aeronautics and Astronautics,* no. AIAA 2017-4535, 2017.

[22] C. O. Johnston, "Shock-Layer Radiation Insights Available Through Flowfield-Property Binning," *AIAA SCITECH 2022 Forum,* no. 2022-2396, 2022.

[23] A. C. Tibere-Inglesse, T. K. West, C. C. Jelloian, N. Q. Minesi, R. M. Spearrin, J. Clarke, L. di Mare, M. McGilvray and B. A. Cruden, "Examination of Mars2020 shock-layer conditions via infrared emission spectroscopy of CO2," *AIAA SCITECH 2023 Forum,* no. 2023-0960, 2023.

[24] P. L. Collen, M. Satchell, L. Di Mare and M. McGilvray, "The influence of shock speed variation on radiation and thermochemistry experiments in shock tubes," *Journal of Fluid Mechanics,* vol. 948, p. A51, 2022.

[25] A. M. Brandis and B. A. Cruden, "Shock Tube Radiation Measurements in Nitrogen," *American Institute of Aeronautics and Astronautics*, no. AIAA 2018-3437, 2018.

A. Appendix: Summary of all shots performed

Table 2: Summary of all shots performed with usable data. check mark indicates good data was obtained for that spectrometer on that shot, blanks indicate data was obtained with some significant issue or deviation from mean values, and crosses indicate no useful data was obtained. The shots in bold are benchmark shots with high quality data, as defined in Ref. [25]

Shot number	**Velocity**	**Pressure**	**Cameras**			
			VUV	Blue	Red	IR
1	6.97	0.10	✓	✓	✓	x
2	5.48	0.10	✓	✓	✓	x
3	**5.84**	**0.10**		✓	✓	✓
4	5.18	0.10		✓	✓	✓
5	**5.21**	**0.10**	✓	✓	✓	✓
6	4.39	0.21		✓	✓	✓
7	4.23	0.21		✓	✓	
8	4.00	0.21	✓	✓	✓	
9	4.11	0.21	✓	✓	✓	x
10	**3.91**	**0.21**	✓	✓	✓	✓
11	4.63	0.21	✓	✓	✓	✓
12	**5.09**	**0.21**		✓	✓	✓
13	5.33	0.21	✓	✓	✓	✓
14	5.20	0.21	✓	✓	✓	✓
15	5.87	0.21	✓	✓		
16	5.39	0.21	✓	✓	✓	✓
17	**5.65**	**0.21**	✓	✓	✓	✓
18	4.39	0.30		✓		✓
19	3.91	0.30	✓		✓	✓
20	3.60	0.30	✓			✓
21	**3.81**	**0.30**	✓	✓	✓	✓
22	3.66	0.30	✓	✓	✓	✓
23	4.44	0.30	✓	✓	✓	✓
24	5.38	0.30	✓	✓	✓	✓
25	**5.18**	**0.30**	✓	✓	✓	✓
26	4.91	0.30	✓	✓	✓	✓
27	3.75	0.40	✓	✓	✓	✓
28	3.43	0.40				✓
29	**3.61**	**0.40**	x	✓	✓	✓
30	3.87	0.40	✓	✓	✓	✓
31	4.03	0.40	✓	✓	✓	✓
32	4.33	0.40	✓	✓	✓	✓
33	4.20	0.40	✓			✓
35	**4.86**	**0.40**	✓	✓		✓
36	5.04	0.40	✓	✓	✓	✓
37	4.66	0.40	✓	✓	✓	

38	3.72	0.65	✓	✓	✓	✓
39	3.94	0.65	✓	✓	✓	✓
40	3.88	0.65	✓	✓	✓	✓
41	4.31	0.65	✓	✓	✓	✓
42	3.51	0.65	✓	✓	✓	
43	**3.50**	**0.65**	✓	✓	✓	✓
44	4.65	0.64	✓	✓	✓	✓
45	**4.82**	**0.64**	✓	✓	✓	✓
46	4.12	0.91	✓	✓	✓	✓
48	**3.55**	**0.90**	✓	✓	✓	x
49	3.47	0.90	✓	✓	✓	✓
52	**3.19**	**1.14**	✓	✓	✓	✓
53	3.13	1.14	✓	✓	✓	✓
54	5.47	1.14	✓	✓	✓	✓
55	4.08	1.99	✓	✓	✓	✓
56	5.29	1.99		✓	✓	✓
57	4.74	4.00	✓	✓	✓	✓
58	4.37	3.98	✓	✓	✓	✓